Data-Driven Parallel Adaptive Control for Magnetic Helical Microrobots With Derivative Structure in Uncertain Environments

Huaping Wang, *Member, IEEE*, Shihao Zhong, Zhiqiang Zheng, Qing Shi, *Senior Member, IEEE*, Tao Sun, Qiang Huang, *Fellow, IEEE*, and Toshio Fukuda, *Life Fellow, IEEE*

***Abstract*—Micron-range untethered, magnetic helical robots have great potential for biomedical applications due to their desirable performance with high flexibility and accuracy in unstructured and confined environments. However, at the microscale, time-varying uncertain disturbances in the environment and electromagnetic system greatly hinder helical microrobot tracking control performance. When a microrobot is replaced or even a derivative version with a slight helical body structure change is used for different tasks, the performance of the original control scheme remarkably decreases or even becomes ineffective. Here, we propose a data-driven optimal integrated controller (D^2-OIC) that realizes precise tracking and transfer control among a series of helical microrobots with derived structures in different situations. The control approach has a parallel structure with nonlinear feedforward and linear feedback controllers. The nonlinear feedforward controller inversely maps the relationship between the electromagnetic field state and the helical microrobot motion state, allowing the helical microrobot to quickly approach the desired motion state. The linear feedback controller effectively adjusts the controller parameters using the virtual reference feedback tuning (VRFT) method, thus eliminating any residual motion errors arising from nonlinear control. By retraining on newly acquired and collected cumulative data with assigned weights, the nonlinear feedforward controller is updated to achieve transfer control among various helical microrobot types. In the experiment, two helical microrobot types performed arbitrary path tracking and obstacle avoidance tasks with tracking errors consistently less than 4% of the microrobot body length, demonstrating the feasibility of the proposed method.**

***Index Terms*—Automation at the microscale, data-driven approach, electromagnetic micromanipulation, magnetic helical micromotor, micron-sized robot.**

I. Introduction

INSPIRED by E. coli, micron-sized robots with helical structures have been developed for rotational propulsion in low Reynolds number (Re) liquid environments utilizing electromagnetic drives to break the spatial and temporal symmetry [1], [2], [3]. Due to their tiny size and controllable movement, helical microrobots are highly expected to be used for biomedical applications in unstructured and confined environments, such as targeted drug delivery and minimally invasive surgery [4], [5]. As the scale decreases dramatically, the scale effect becomes significant, where the uncertain perturbation in both the environment and electromagnetic system may greatly hinder the tracking control performance of a helical microrobot [6], [7], [8], [9], [10]. With time-varying factors, such as thermal fluctuations, Brownian perturbations, surface adhesive force, and steric interactions in a liquid environment, a helical microrobot suffers from strong diffusivity, which risks random deviations from the preset path [11], [12]. To accurately follow a path, a helical microrobot is embedded with soft magnetic materials and is axially magnetized for actuation [13]. However, due to the difficulty of controlling the distribution of magnetic materials in the robot body at the microscale, the magnetization direction does not always coincide with the preset axis, resulting in a tumbling motion of the helical microrobot [14]. To dynamically compensate for motion in unexpected situations, the electromagnetic system frequently changes the current to generate different magnetic fields. However, due to the inherent hysteresis and local distortion limits of updating the magnetic field, the motion may lag behind the control signal and be regionally uncontrollable [15]. Therefore, accurate motion control of helical microrobots remains a significant challenge.

Manuscript received 3 November 2023; revised 29 December 2023; accepted 3 March 2024. Date of publication 27 March 2024; date of current version 18 June 2024. This work was supported in part by the National Key Research and Development Program of China under Grant 2023YFB4705400; in part by the National Natural Science Foundation of China under Grant 62073042, Grant 62222305, and Grant U22A2064; in part by the Beijing Natural Science Foundation under Grant 4232055; and in part by the Science and Technology Innovation Program of Beijing Institute of Technology under Grant 2022CX01019. This article was recommended by Associate Editor C. Yang. *(Corresponding author: Zhiqiang Zheng.)*

Huaping Wang is with the Key Laboratory of Biomimetic Robots and Systems, Ministry of Education, Beijing Institute of Technology, Beijing 100081, China (e-mail: wanghuaping@bit.edu.cn).

Shihao Zhong is with the Intelligent Robotics Institute, School of Mechatronical Engineering, Beijing Institute of Technology, Beijing 100081, China (e-mail: 3120235409@bit.edu.cn).

Zhiqiang Zheng is with the Intelligent Robotics Institute, School of Mechatronical Engineering, Beijing Institute of Technology, Beijing 100081, China, and also with the Department of Physical Intelligence, Max Planck Institute, 70569 Stuttgart, Germany (e-mail: zheng@is.mpg.de).

Qing Shi, Tao Sun, Qiang Huang, and Toshio Fukuda are with the Beijing Advanced Innovation Center for Intelligent Robots and Systems, Beijing Institute of Technology, Beijing 100081, China (e-mail: shiqing@bit.edu.cn; sun-tao@bit.edu.cn; qhuang@bit.edu.cn; tofukuda@nifty.com).

This article has supplementary material provided by the authors and color versions of one or more figures available at https://doi.org/10.1109/TSMC.2024.3374071.

Digital Object Identifier 10.1109/TSMC.2024.3374071

The inevitable uncertain perturbation makes it difficult to describe the interaction between a helical microrobot and the local environment with an accurate dynamic model [16]. Thus, most traditional nonlinear closed-loop control methods cannot be applied for motion control. Instead, linear model-free feedback control methods are commonly used [7], where the specific control parameters are adjusted to compensate or even eliminate the motion error according to the experience for different tasks. Barbot et al. [17] tuned the PID algorithm parameters based on orientation error to control a single helix microrobot following a linear path in a microfluidic chip. Lee et al. [18] designed control parameters based on error dynamics to reduce random drift during motion and shorten the time to reach the target point of a needle-like single-helix microrobot. Cao et al. [19] designed and rectified a linear extended state observer (ESO) to achieve an anchor-like single-helix microrobot following a predetermined path in a Y-shaped microchannel. Zhong et al. [20] successfully achieved dynamic path following of a spiral microrobot by fine-tuning the parameters of a controller that is seamlessly integrated with both geometric and model-free techniques. However, the control parameters for diverse tasks are significantly different in real applications. When a microrobot is replaced or even a derivative version with a slight change in the helical body structure is used for different tasks, the performance of the original control scheme will remarkably decrease or even become ineffective with unknown structural information [21]. Thus, the control parameters need to be calibrated all over again, which is a time-consuming and experience-dependent manually intensive process. A motion control algorithm with fewer tuned parameters or even without manual adjustment is meaningful to greatly enhance the flexibility and scalability for the use of helical microrobots.

A data-driven approach can effectively handle a nonlinear system by directly creating a mapping model between the input and output state ignoring the influence from different operation mechanisms [22], [23], [24]. In [25], a novel integrated framework including the sensing, navigation and control is proposed for an autonomous mobile manipulator, it is very practical for the mobile manipulation scenarios without knowing the exact parameters of the whole-body dynamics. In [26] and [27], excellent works on model predictive control and tube-based predictive control have been developed for single robot and multiple robots, outstanding control performance is verified to such control approaches are practical in the constrained unmanned systems. For magnetic helical robot, researchers have designed nonlinear controllers for feedforward control based on data-driven methods, improving the control performance without the need for additional control parameters. Wu et al. [28] proposed an automatic orientation compensation solution based on the RBF-BP algorithm to create a mapping relationship between the theoretical and actual motion directions of a centimeter-sized helical robot. Xu et al. [29] directly created a mapping model between the motion direction and the magnetic field direction for the feedforward control of a centimeter-sized helical robot based on the RBF-BP algorithm, which improved the control system response speed. If a data-driven method is applied in the feedback control of a helical structure at the microscale, manual adjustment of the control parameters will be largely avoided to improve the efficiency and scalability of the control algorithm. Consequently, when the environment or robot body structure changes, data-driven methods only need to recapture and recalibrate the new training data to update the mapping relationship. However, because the available observation and sensing tools are limited at the microscale, the acquisition of training data is tedious, inefficient, and sometimes not accurate with considerable noise. To further simplify the controller design process and improve control flexibility, a data-driven control method capable of reusing the collected cumulative data to train a series of helical microrobots with derived structures for different situations is still needed.

This article proposes a data-driven optimal integrated control (D^2-OIC) method with parallel nonlinear feedforward and linear feedback controllers, which realizes precise tracking and transfer control among a series of helical microrobots with derived structures in different situations based on the dynamic complement of two controllers. To realize linear approximation of a nonlinear electromagnetic system and facilitate the helical microrobot quickly approaching the desired motion state, an inverse mapping model between the magnetic field state and the robot motion state is developed as a nonlinear feedforward controller. To improve the closed-loop control performance of the helical microrobot motion, the parameters of the linear feedback controller are corrected offline in a one-shot process using the experimental data. Nonlinear and linear controllers dynamically complement each other to form the D^2-OIC framework. Within the control framework, the nonlinear controller dynamically updates the mapping relationship by retraining on the newly acquired and collected cumulative training data with assigned weights. The control approach is validated using two types of helical microrobots following arbitrary planar paths and performing obstacle avoidance-like interaction tasks in a distinct heterogeneous medium with movable impurity obstacles. This approach is promising for the motion control of a microrobot with derived structures for different tasks. The primary contributions of this study are as follows.

1) By utilizing a data-driven method, the establishment of a direct mapping model effectively resolves the problem of accurately modeling the magnetic field state and motion state of a microrobot, which is subject to unknown dynamics and time-varying perturbations at the microscale.
2) The control gain of the D^2-OIC method can be adjusted by iterative optimization to obtain the optimal learning control scheme using only the I/O data of the nonlinear electromagnetic actuated microrobot system, which simplifies the controller design process and improves control flexibility.
3) If a derivative version of the microrobot is utilized for different tasks, the transfer scheme ensures that the model-free D^2-OIC method does not require frequent manual fine-tuning or recalibration of the entire set of control parameters.

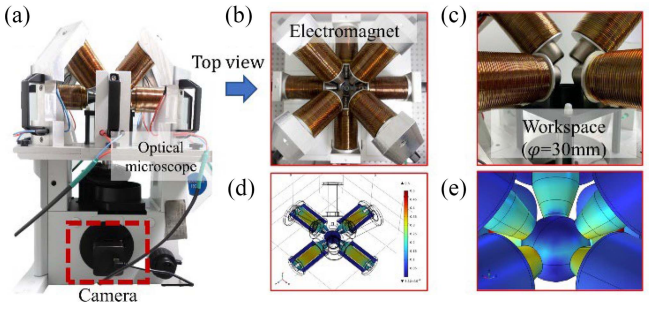

Fig. 1. Electromagnetic system. (a) Eight-stage solenoid system, optical microscope, and digital camera. (b) View from the top of the eight-stage solenoid system. (c) View of the working area. (d) and (e) Simulation results demonstrate the distribution of flux density within the workspace when a unit current is applied.

The remainder of this article is organized as follows. Section II presents the custom-built electromagnetic coil system. Section III presents the dynamics and kinematics model of the helical microrobot. Section IV proposes the path-tracking controller based on the D^2-OIC approach. Experimental examples are provided in Section V, and the results are analyzed. Section VI concludes this article.

II. Electromagnetic System Design

Fig. 1 illustrates a custom electromagnetic system integrated beneath an optical microscope. The system comprises eight iron core coils, each powered by programmable current drivers, capable of generating an arbitrary magnetic field within a spherical working volume of 30 mm in diameter. The four-stage coil is placed orthogonally in the horizontal plane, and the remaining four stages are located at the upper level of the horizontal plane at an angle of 45°. Our designed electromagnet system can generate a uniform magnetic field in a spherical workspace with a maximum magnetic field intensity of 30 mT, a magnetic field accuracy of 0.1 mT, and a maximum magnetic field gradient of 1.6 T/m. The motion of the helical microrobot is monitored via an inverted lens attached to the optical microscope and a digital camera.

Assuming a linear change in the magnitude of the magnetic field within the spherical region of interest, the magnetic field at any point $\boldsymbol{P}$ is the sum of contributions from all eight electromagnetic coils [13]

$$\boldsymbol{B}(\boldsymbol{P}) = \|\boldsymbol{B_0}(\boldsymbol{P})\| D_{\text{coils}} \boldsymbol{C} \tag{1}$$

where $\|\boldsymbol{B_0}(\boldsymbol{P})\|$ is the binary parametrization of the flux density vector generated per unit current, D_{coils} is the matrix describing the spatial positions of the components in an electromagnetic system, and $\boldsymbol{C}$ is the vector–matrix of currents passing through the eight-level coil.

Equation (1) describes an underdetermined system. D_{coils} is a 3×6 matrix. A pseudoinverse is calculated which can obtain the least norm solution [refer to (2)], minimizing the norm of the current and consequently reduces power consumption

$$\boldsymbol{C} = \left(G^{\top} \cdot G\right)^{-1} \cdot G^{\top} \cdot \boldsymbol{B} \tag{2}$$

where $G = \|\widetilde{\boldsymbol{B}}_{\boldsymbol{0}}(\boldsymbol{P})\| D_{\text{coils}}$.

III. Modeling

Under ideal conditions, the helical microrobot align its axis of magnetization with the external rotating magnetic field, making the microrobot rotate in sync with the rotating field. The rotational motion causes the helical microrobot to generate thrust and produce velocity. To implement the rotating magnetic field, we can calculate the magnetic field in real time at any instant using the following rotation matrix [30]

$$\boldsymbol{B} = R\boldsymbol{B_{ini}}$$
$$R = \begin{bmatrix} \cos\theta + \boldsymbol{e_x}^2(1-\cos\theta) & \boldsymbol{e_x e_y}(1-\cos\theta) - \boldsymbol{e_z}\sin\theta & \boldsymbol{e_x e_z}(1-\cos\theta) + \boldsymbol{e_y}\sin\theta \\ \boldsymbol{e_x e_y}(1-\cos\theta) + \boldsymbol{e_z}\sin\theta & \cos\theta + \boldsymbol{e_y}^2(1-\cos\theta) & \boldsymbol{e_y e_z}(1-\cos\theta) - \boldsymbol{e_x}\sin\theta \\ \boldsymbol{e_x e_z}(1-\cos\theta) - \boldsymbol{e_y}\sin\theta & \boldsymbol{e_y e_z}(1-\cos\theta) + \boldsymbol{e_x}\sin\theta & \cos\theta + \boldsymbol{e_z}^2(1-\cos\theta) \end{bmatrix} \tag{3}$$

where R is a three-dimensional (3-D) rotation matrix, θ is the rotation angle of the magnetic field, and the rotation axis of the magnetic field at the x–y–z coordinates can be represented as a vector $\boldsymbol{e_{x,y,z}}$. $\boldsymbol{B_{ini}}$ is the magnetic field vector at beginning. Equations (2) and (3) can be utilized to calculate the current that needs to be supplied to each coil, once the magnetic field vector rotating around any axis is acquired

$$\boldsymbol{C} = (\|\boldsymbol{B_0}(\boldsymbol{P})\| R)^{\dagger} \boldsymbol{B} = \|\boldsymbol{B_0}(\boldsymbol{P})\|^{-1} R^{\boldsymbol{T}} \left(R \times R^{\boldsymbol{T}}\right)^{-1} \boldsymbol{B}. \tag{4}$$

A. Propulsion Model

In a low Reynolds number liquid phase environment, the Stokes equations govern that a linear relationship exists between the speed and rotational frequency of the propeller motion, as well as the externally applied force and torque, which means when an external force $\boldsymbol{F_{ex}}$ and an external torque $\boldsymbol{T_{ex}}$ are applied to the helical microrobot, it moves with linear velocity $\boldsymbol{V}$ and angular velocity $\boldsymbol{\omega}$. The equations governing the motion of a linear single-helix machine are given by reference

$$\begin{bmatrix} \boldsymbol{V} \\ \boldsymbol{\omega} \end{bmatrix} = \begin{bmatrix} a & b \\ b & c \end{bmatrix} \begin{bmatrix} \boldsymbol{F_{ex}} \\ \boldsymbol{T_{ex}} \end{bmatrix}. \tag{5}$$

Parameters a, b, and c are encapsulated the structure of the helical microrobot and environmental characteristics [31].

A complex helical structure can be viewed as several simple linear helical structures. Therefore, a mathematical swimming model of the complex helical machine is deduced

$$\boldsymbol{V}/\boldsymbol{\omega} = -\sum b_i^* / \sum a_i^*$$
$$\text{s.t.} \quad \boldsymbol{\omega} \le \boldsymbol{\omega_{step-out}} \tag{6}$$

where $\boldsymbol{\omega_{step-out}}$ denotes the step-out frequency. If the frequency of the external rotating magnetic field is lower than the critical value, the helical microrobot can synchronize with the rotation of the magnetic field. However, synchronization is not possible if the frequency exceeds this critical threshold. a_i^* and b_i^* are the symmetric matrix parameters of each linear helical microrobot constitutes the complex helical microrobot.

B. 2-D Helical Kinematics

General assumption at low Re, the kinematic equation for a helical microrobot can be decomposed into the angular

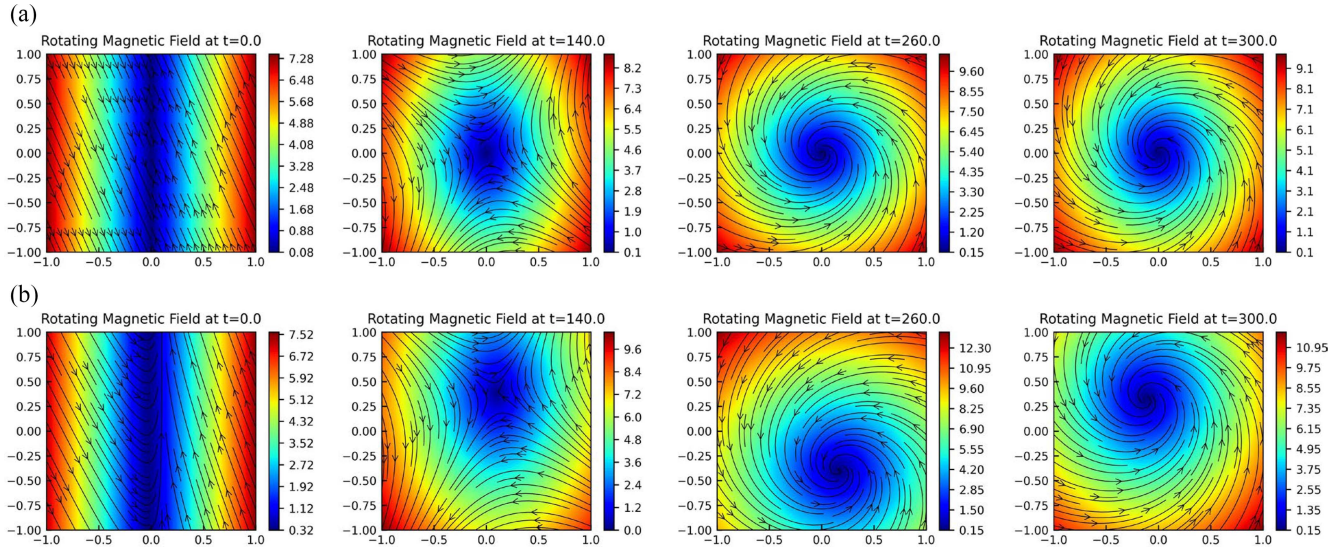

Fig. 2. Rotating magnetic field in 2-D simulation diagram. (a) Under ideal conditions, magnetic field states at different sampling times. (b) Under the influence of random disturbance, magnetic field states at different sampling times.

frequency of rotation producing the forward velocity, whereas the time derivative of the rotational axis results in the steering velocity. Nevertheless, in most scenarios, factors, such as friction, boundary forces, thermal fluctuations, Brownian perturbations, surface adhesive force, and steric interactions, cannot be ignored, making the motion of the helical microrobot more complex, and coupling to analyze. Fig. 2 shows that the Gaussian noise causes a shift in a rotating magnetic field.

The *Spintop* motion is an optimized solution for the motion of a helical microrobot on surfaces underwater at the microscale, which is essentially a friction-based motion so that the helical microrobot only touches the surface at the tip. Currently, it is not possible to analyze a precise model of *Spintop* motion that can accurately estimate the quantitative behavior of a helical microrobot [17]. Indeed, due to the chirality of a helical microrobot, the rotational motion (the viscous propelling force) is nonlinearly coupled to its translational motion (the surface friction). At the microscale, a helical microrobot cannot be ideally aligned along its main axis perpendicular to the magnetic field due to the magnetization problem. Additionally, the motion of the helical microrobot exhibits a wobbling phenomenon due to its unsatisfactory magnetization direction. This is further exacerbated by the *Spintop* motion caused by the irregular structure of the microrobot.

With the helical microrobot design and actuation method, a helical microrobot is limited to nonholonomic motion (see Fig. 3). The kinetic equation of the helical microrobot is designed as follows:

$$\dot{\boldsymbol{X}} = \begin{bmatrix} \dot{\boldsymbol{x}}_{\boldsymbol{R}} \\ \dot{\boldsymbol{y}}_{\boldsymbol{R}} \\ \dot{\boldsymbol{\theta}}_{\boldsymbol{R}} \end{bmatrix} = \begin{bmatrix} F(f,\varphi)\cos(\varphi)\cos(\theta_R) + D_x \\ F(f,\varphi)\cos(\varphi)\sin(\theta_R) + D_y \\ \omega_R + D_r \end{bmatrix} \tag{7}$$

where $\boldsymbol{P} = [\boldsymbol{x}_{\boldsymbol{R}}, \boldsymbol{y}_{\boldsymbol{R}}]$ is the position vector of the helical microrobot and $\boldsymbol{\omega}_{\boldsymbol{R}}$ is the steering speed of the helical microrobot. The propulsion speed $\boldsymbol{V} = [\dot{\boldsymbol{x}}_{\boldsymbol{R}}, \dot{\boldsymbol{y}}_{\boldsymbol{R}}]$ generated by a magnetic

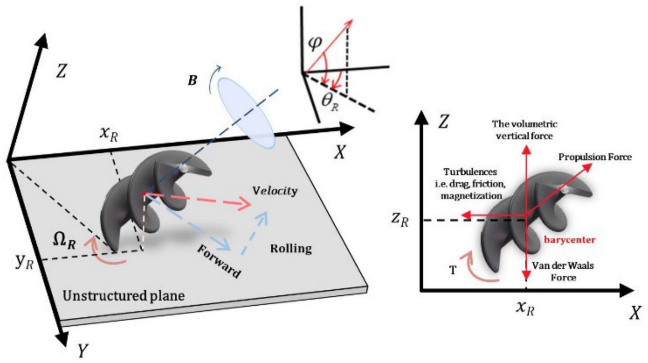

Fig. 3. Kinematics analysis of a helical microrobot actuated by a rotating magnetic field under turbulence. The robot exhibits a coupling of forward swimming and lateral rolling.

field is depended on the magnetic field rotation frequency f and pitch angle φ. $F(f, \varphi)$ is a nonlinear function that increases monotonically, which depends on the physical parameters of the helical microrobot and environmental factors, such as thermal fluctuations, Brownian perturbations, surface adhesive force, and steric interactions in a liquid environment, and may have different forms. $\boldsymbol{\theta}_{\boldsymbol{R}}$ is the motion orientation. $D_{x,\ y,\ r}$ are the decomposed into axial deviation which caused by uncertain disturbances. $\boldsymbol{V}_{\boldsymbol{p}}$ is the projection point of the propulsion speed on the X–Y image plane.

IV. Controller Design

When the path is known, the helical microrobot path-tracking task can be reduced to two control quantities: 1) the direction of the helical microrobot motion and 2) the distance from the target path. Disturbances directly affect motion direction control, so cascade control is used. The outer loop serves to dynamically compute the desired direction of motion ($\boldsymbol{n}^*$), while the inner loop is responsible for offsetting any

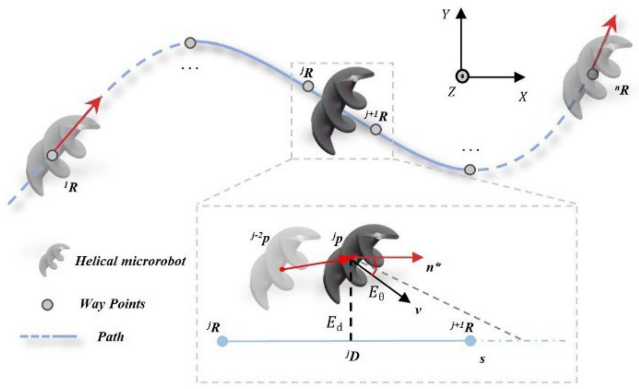

Fig. 4. Modeling for arbitrary path tracking.

deviation between the actual and desired directions of motion resulting from disturbances.

A. Path Tracking

An arbitrary path can be represented by a set of points $\mathscr{R} = \{R_1, R_2, \ldots, R_j, \ldots, R_k\}$. When tracking an arbitrary plane, the tracking process can be viewed as minimizing the distance error and yaw error throughout the mission (see Fig. 4). The core of the controller is to realize the motion control task with high accuracy and automation, making the motion state $\boldsymbol{state(t)}$ of the helical microrobot converge to the desired value $\boldsymbol{state^*(t)}$

$$\boldsymbol{state^*(t)} - \boldsymbol{state(t)} \overset{\boldsymbol{u(t)}}{\rightarrow} 0, \text{ when } t \rightarrow \infty \tag{8}$$

$$\boldsymbol{sate(t)} = \begin{bmatrix} E_\theta(t) \\ E_d(t) \end{bmatrix} \tag{9}$$

where E_θ and E_d are the yaw error and distance error, respectively.

For the jth segment of the planner path, which is the segment nearest to the helical microrobot, ${}^{j}\boldsymbol{P}$ is the position vector of the helical microrobot. ${}^{j}\boldsymbol{D}$ is the projection of ${}^{j}\boldsymbol{P}$ onto the jth segment. Without considering the distance error, the optimal motion direction vector $\boldsymbol{n^*}$ for the helical microrobot location is determined by

$$\boldsymbol{n^*} = \frac{{}^{j}\boldsymbol{R}^{j+1}\boldsymbol{R}}{\left\|{}^{j}\boldsymbol{R}^{j+1}\boldsymbol{R}\right\|} \tag{10}$$

$$E_\theta = \cos^{-1}\frac{{}^{j}\boldsymbol{R}^{j+1}\boldsymbol{R}\ {}^{j-2}\boldsymbol{P}^{j}\boldsymbol{P}}{\left\|{}^{j}\boldsymbol{R}^{j+1}\boldsymbol{R}\right\|\left\|{}^{j-2}\boldsymbol{P}^{j}\boldsymbol{P}\right\|} \tag{11}$$

$$E_d = |{}^{j}\boldsymbol{P}\ {}^{j}\boldsymbol{D}|\text{sign}\left(\sin {}^{j}\boldsymbol{P}^{j+1}\boldsymbol{R}\right) \tag{12}$$

where ${}^{j-2}\boldsymbol{P}\ {}^{j}\boldsymbol{P}$ represents the actual direction of motion, ${}^{j}\boldsymbol{R}^{j+1}\boldsymbol{R}$ represents the expected direction of motion, and ${}^{j}\boldsymbol{P}\ {}^{j}\boldsymbol{D}$ represents the lateral error.

A canonical path-tracking image-based visual servo control plan, which has been proven through experiments, guarantees asymptotic stability in most situations (see Fig. 4). In addition, since a helical microrobot moves in a plane parallel to the camera plane, interaction matrix estimation is not needed [32].

B. Position Control

Without considering the yaw error, the larger the distance error is, the greater the magnetic field rotation axis is biased toward the target path. The line tangent to the nearest path point intersects at a distance s from the barycenter of the helical microrobot (see Fig. 4)

$$E_\theta = \arctan\frac{E_d}{s} = \arctan\frac{kE_d}{v_f} \tag{13}$$

where s can be expressed by the magnetic field propulsion speed v_f with the gain parameter k. As the lateral error increases, a direction of the magnetic field rotation axis that points directly to the desired path is generated.

The rate of change of the lateral error can be obtained

$$\dot{\boldsymbol{E}}_{\boldsymbol{d}} = -v_f \sin\sigma \tag{14}$$

where σ is the angle between the forward direction and the rotation axis and $\sin\sigma$ is calculated by

$$\sin\sigma = \frac{E_d}{\sqrt{s^2 + {E_d}^2}} = \frac{kE_d}{\sqrt{{v_f}^2 + (kE_d)^2}} \tag{15}$$

$$\dot{\boldsymbol{E}}_{\boldsymbol{d}} = \frac{-kE_d}{\sqrt{1 + \left(kE_d/v_f\right)^2}}. \tag{16}$$

When the distance error is very small, $E_d = E_d(0)\exp^{-kt}$. Thus, the distance error converges to 0 and the gain k determines the rate of convergence.

The speed at which the helical microrobot propels itself is dependent on the function $F(f, \varphi)$. To achieve speed-independent path-following tasks without loss of generality, we fix the pitch angle and the magnetic field rotation frequency and initially set $k = 1$ as a constant, to realize speed-independent path-tracking control. Therefore, the desired guiding direction is

$$\boldsymbol{n^*} = \frac{{}^{j}\boldsymbol{R}^{j+1}\boldsymbol{R}}{\left\|{}^{j}\boldsymbol{R}^{j+1}\boldsymbol{R}\right\|} + k\frac{{}^{j}\boldsymbol{P}\ {}^{j}\boldsymbol{D}}{\left\|{}^{j}\boldsymbol{P}^{j}\boldsymbol{D}\right\|}. \tag{17}$$

C. D2-OIC Method for Steering Control

The D^2-OIC method with parallel nonlinear feedforward and linear feedback controllers realizes precise tracking and transfer control among a series of helical microrobots with derived structures in different situations based on the dynamic complement of two controllers. To realize linear approximation of a nonlinear electromagnetic system and facilitate the helical microrobot quickly approaching the desired motion state, an inverse mapping model between the magnetic field state and the robot motion state is developed as a nonlinear feedforward controller C^{nl}. To improve the closed-loop control performance of the helical microrobot motion, the parameters of the linear feedback controller C^{lin} are corrected offline in a one-shot process using the experimental data. Nonlinear and linear controllers dynamically complement each other to form the D^2-OIC framework.

We remotely steer the helical microrobot by adjusting the magnetic rotation field. System S includes an eight-stage solenoid system and end effector helical microrobots. The

input to the entire system θ_r is the desired direction of motion, and the system output is the corresponding action of the helical microrobot. C^{nl} is designed using support vector regression (SVR). C^{lin} is designed using the virtual reference feedback tuning (VRFT) method.

1) Nonlinear Controller Design: In the field of nonlinear control, inverse system control has been widely studied and applied. Therefore, the motion processes of helical microrobots with inestimable perturbations cannot be modeled mechanically, which means that an inverse model of the system cannot be obtained using a traditional mathematical analysis method. However, SVR is a machine learning method with solid theory and good practical results. Compared with traditional neural network methods [24], it has a series of advantages: it can automatically optimize the model structure without relying on a priori knowledge, it performs better on small sample sets, it has theoretical guarantees for generalization, it has a unique optimal solution, and it has no local minima problem [33]. SVR has been widely used to estimate the dynamics of moving parts, such as robotic arms [34] and motors [35]. Therefore, this study designs a direct inverse feedback controller based on SVR.

The purpose of C^{nl} is to make the tracking error $e_t \doteq \|\theta_r - y_t^{nl}\|_\infty$ small enough within the time series, where y_t^{nl} is the output of system S under the action of C^{nl}.

This study establishes an end-to-end mapping of system signals. The system state data $\boldsymbol{O}$ are used as output parameters, and the corresponding action of the helical microrobot $\boldsymbol{X}$ is used as input parameters. Such a regression problem can also be regarded as a robotic imitation learning-based controller

$$\boldsymbol{X}: \begin{bmatrix} X_{\text{microrobot}} \\ Y_{\text{microrobot}} \end{bmatrix} \rightarrow \boldsymbol{O}: \begin{bmatrix} X_B \\ Y_B \end{bmatrix}. \tag{18}$$

$D = \{(\boldsymbol{X}_i, \boldsymbol{O}_i), i = 1, 2, \ldots, n\}$ is a training sample set, where $X_i, O_i \in R$. SVR maps the input data to the higher feature space, transforms the nonlinear problem into a linear problem, and establishes the linear regression equation

$$\boldsymbol{O} = W^T \vartheta(\boldsymbol{X}) + \delta \tag{19}$$

where $\vartheta(\boldsymbol{X})$ maps X_i to the high-dimensional feature space. W is the weight of $\vartheta(\boldsymbol{X})$, and δ is the bias term of the SVR equation.

To minimize the structural risk, the appropriate W and δ are found within the margin constraint, i.e., minimizing (20) with a penalty term. The goal is to find a function that has an appropriate estimate deviation ε, besides, is as fat as possible

$$\begin{aligned} \min_{W,b,\xi_i,\xi_i^*} \quad & \frac{1}{2}\|W\|^2 + C\sum_{i=1}^{l}(\xi_i + \xi_i^*) \\ \text{s.t.} \quad & \boldsymbol{O}_i - W^T\phi(\boldsymbol{X}_i) - \delta \le \varepsilon + \xi_i \\ & W^T\vartheta(\boldsymbol{X}_i) + \delta - \boldsymbol{O}_i \le \varepsilon + \xi_i^* \\ & \xi_i, \xi_i^* \ge 0, i = 1, 2, \ldots, l \end{aligned} \tag{20}$$

where $i \in [1, n]$ represents the data sequence, C is the regularization parameter, and ξ_i and ξ_i^* are the relaxation variable.

This is a convex quadratic optimization problem, introducing the Lagrange multipliers α_i and α_i^*, which can be solved using its dual problem (21)

$$\begin{aligned} \min_{\alpha,\alpha^*} \quad & \frac{1}{2}\sum_{i=1}^{l}\sum_{j=1}^{l}(\alpha_i^* - \alpha_i)\left(\alpha_j^* - \alpha_j\right)K_{ij} \\ & + \varepsilon\sum_{i=1}^{l}(\alpha_i + \alpha_i^*) - \sum_{i=1}^{l} O_i(\alpha_i^* - \alpha_i) \\ \text{s.t.} \quad & \sum_{i=1}^{l}(\alpha_i^* - \alpha_i) = 0 \\ & 0 \le \alpha_i^{(*)} \le C, i = 1, 2, \ldots, l \end{aligned} \tag{21}$$

where $K(x_i, x_j)$ is the kernel function.

The output of the nonlinear controller u_t^{nl} is completely determined using (22). The approximate function is

$$U^{nl} = \sum_{i=1}^{l} \mu_i K(\boldsymbol{X}, \boldsymbol{X}_i) + \delta \tag{22}$$

where $\mu_i = (\alpha_i - \alpha_i^*)$ represents the weight of the kernel.

2) Linear Controller Design: The VRFT method [22], [36] is a data-driven tuning method. In this study the VRFT is used to design a feedback controller. The "virtual reference" principle is based on experimental data to design the C^{lin} without identifying any system model (see Fig. 5). The goal of C^{lin} was to improve the closed-loop control performance of the helical microrobot motion.

Based on the VRFT, the desired behavior of the closed-loop magnetic helical microrobot system S equals to a linear asymptotic stability model M_r. On the basis of [37], the closed-loop system does not need to be matched exactly to the reference model, since the VRFT method will provide the closest approximation to the desired closed-loop system behavior.

Given the measurement output signal y_t, the virtual reference signal r_{vt} is calculated through ${M_r}^{-1}$, which can be computed using the available experimental data set of the microrobot system under C^{nl}. In other words, the optimal controller of the closed-loop system M_r, giving u_t^{lin} as the output of C^{lin} when fed by the virtual error $e_{vt} = r_{vt} - y_t$.

C^{lin} is defined by the extended PID control law

$$u_t^{\text{lin}} = u_{t-1}^{\text{lin}} + \sum_{i=0}^{n_\theta} \chi_i e_{vt-i} \tag{23}$$

where e_v is the feedback error, $n_\theta = 1, 2, 3$ is the order of C^{lin}, and χ_i is the parameter.

The magnetically driven helical microrobot system is considered an SISO system whose input signal is the rotating magnetic field state $U \in (-\pi, \pi]$, the output signal is the corresponding behavioral state $Y \in (-\pi, \pi]$. of the helical microrobot, and ξ_t is a bounded turbulence signal containing both process and measurement noise. The magnetic helical microrobot system model is unknown, but a series of measurement data $\mathscr{D}$ can be obtained experimentally

$$\mathscr{D} \doteq \{\widetilde{u}_t, \widetilde{y}_t\}_{t=T}^{0} \tag{24}$$

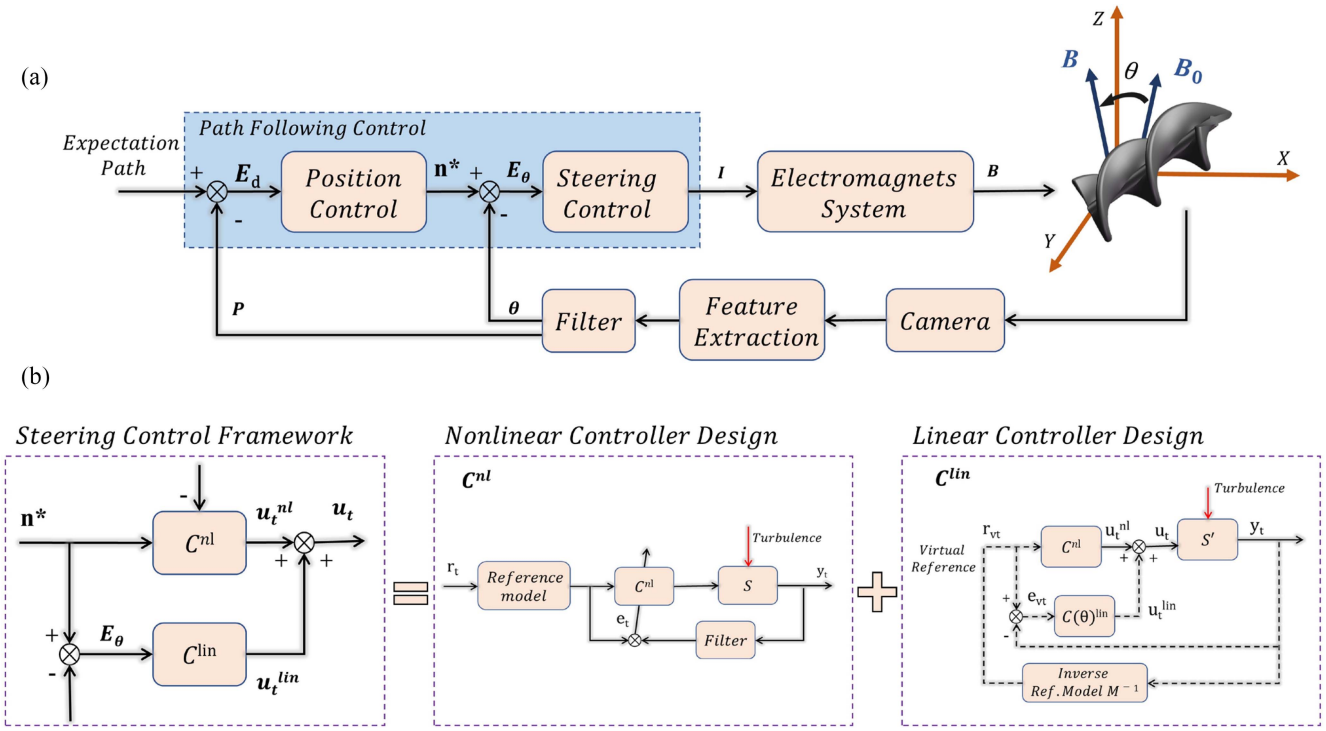

Fig. 5. (a) Schematic representation of the cascade controller based on the D2-OIC approach. (b) Schematic representation of the steering controller. The design of the steering controller involves a nonlinear controller based on SVR and a linear controller that utilizes VRFT rectification.

where $\widetilde{u}_t$ and $\widetilde{y}_t$ are the I/O data of the helical microrobot system S in the actual experiment, respectively.

With a settling time of Ts, C^{lin} shape the $r(t)$-to-$y(t)$ step response to be similar to that of a first-order linear system $M_r(s) = (Ts+1)^{-1}$.

Let $\widetilde{u}_t$ be the input data set and u_t^{nl} from the offline filtering of r_{vt} and $\widetilde{y}_t$ with C^{nl} derived in *Nonlinear Controller Design* section. Feed (offline) C^{nl} with r_{vt} to obtain u_t^{nl}. The virtual linear input for the system $u_t^{\text{lin}} = u_t - u_t^{nl}$.

As a result, the problem of designing the steering control can be transformed into an identification problem. This involves identifying the optimal controller with a designated structure in (25), which includes a parameter vector

$$J_\theta = \underset{\vartheta \in \mathbb{R}^{n\theta}}{\operatorname{argmin}} \left\| \left(\widetilde{u} - \widetilde{u}^{nl}\right) - C^{\text{lin}}(\theta) e_v \right\|_2^2. \tag{25}$$

D. Controller Update Method

The drag coefficient and other resistances vary for different helical microrobot shapes and orientations. As the helical microrobot structure changes, its kinetic model also changes. Therefore, a microrobot plant may become unstable if the learning control gain is not delicately calibrated [24]. For this reason, we propose an update method based on SVR calibration to meet the penetration of D^2-OIC. Knowledge transfer is used to accelerate the learning of inverse dynamic models of different robot morphologies, in which robots share and reuse data collected by preexisting robots.

To dynamically calibrate the learning control gain [38], we consider the data collected from the existing experimental helical microrobot sample to be more important than old data.

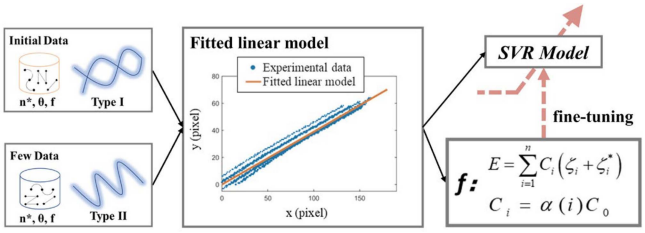

Fig. 6. Updating the nonlinear feedforward controller based on SVR parameter calibration.

Therefore, the penalty for unspecified sense errors in the new sample data is heavier (see Fig. 6)

$$E = \sum_{i=1}^{n} C_i\left(\zeta_i + \zeta_i^*\right) \tag{26}$$

$$C_i = \alpha(i) C_0 \tag{27}$$

where $\alpha(i)$ is the weighting function and C_0 is the initial regularization parameter.

In our adaptive SVR algorithm, rather than a constant value, the regularization constant C adopts a weight function. The weight of a new sample point is equal to α, while the weight of an old sample point in its vicinity is equal to $(1-\alpha)$.

V. Experiment

To verify the stability and controllability of our method, a set of path-tracking tasks were designed.

Preliminary Preparation: All experiments were performed in circular Petri dishes ($r = 15$ mm) with helical microrobots at the bottom. The Petri dishes contained an appropriate

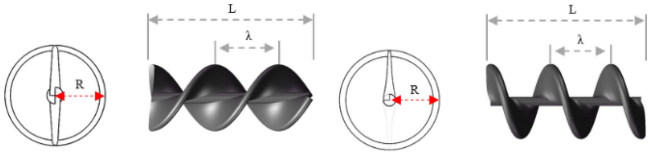

Fig. 7. Side- and front-view drawings of the TS (left) and HS (right) with design parameters.

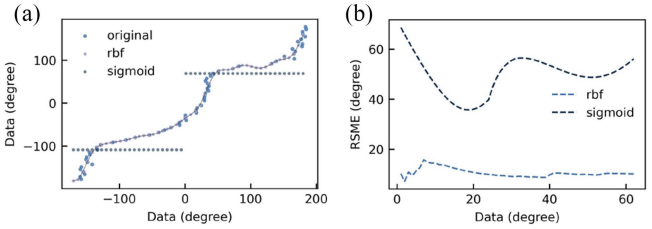

Fig. 8. (a) Inverse motion model based on SVR estimation for the TS. The blue, purple, and gray dots represent the test, the RBF kernel-based prediction, and the sigmoid kernel-based prediction data, respectively. (b) Root-mean-square error between predicted and tested data.

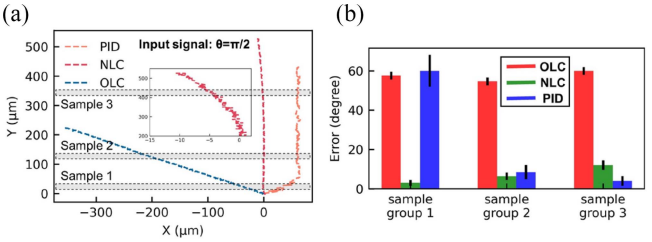

Fig. 9. (a) Trajectory of the TS under step signal stimulation with different controllers: open-loop controller (blue curve), nonlinear controller based on SVR (red curve), and PID controller (orange curve). (b) Three sets of offset errors at different times.

amount of deionized (DI) water with a viscosity at room temperature of 4.9 centipoises. The Petri dishes were placed inside the spherical working area of the homemade eight-stage coil drive system, perpendicular to the top of the observing setup. The imaging system operated at 30 frames/s, ensuring accurate and efficient real-time visual feedback. As the helical microrobots followed the path, their position and velocity were collected by processing image frames using the standard OpenCV library. Our automated experimental platform allows physical experiments to be conducted with minimal human intervention, reducing disturbances on the robot and test surfaces caused by human interaction.

A. Robot Design and Fabrication

We use biocompatible hydrogel materials to create two types of helical microrobots. Additional manufacturing details can be found in our previous work [39]. Then, the helical microrobot was placed in a homemade magnetization device and a uniform magnetic field of 0.4 T was used to magnetize the helical microrobot along its easy axis.

Our study involved the design of two distinct types of magnetic helical microrobots, which represent one of the most extensively researched categories, a single twist-type screw (TS) and a single-helix-type screw (HS). Their geometric parameters are defined as shown in Fig. 7, including the length

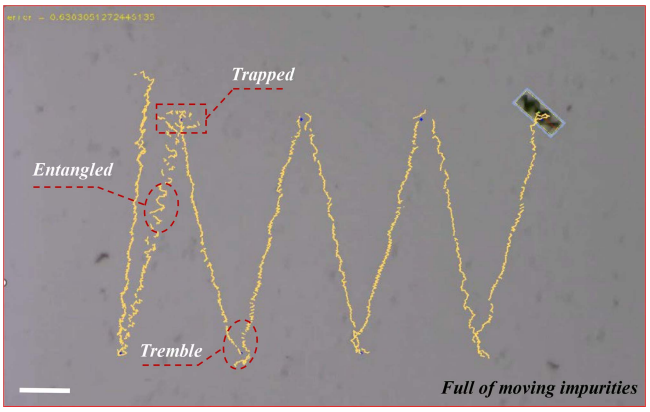

Fig. 10. TS implements path tracking in heterogeneous media. The yellow lines are the TS trajectories. The scale bar is 65 μm.

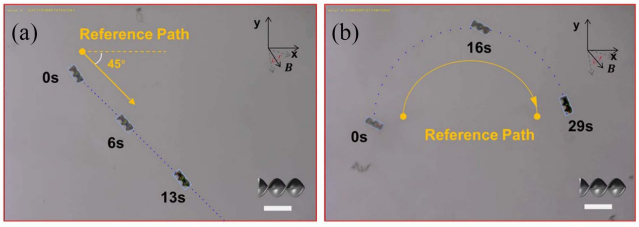

Fig. 11. Line and curve path-following experimental results of TS. (a) Tracking result of the straight-line path at different time instants. (b) Tracking result of the curve path at different time instants. The scale bar is 65 μm.

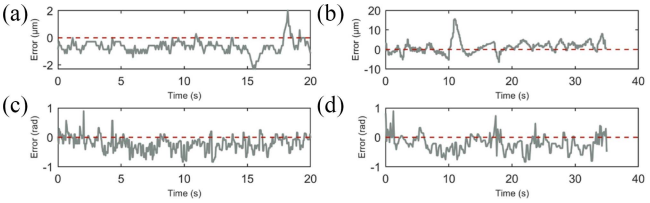

Fig. 12. (a) and (b) Distance error. (c) and (d) Yaw error.

of the helical microrobot ($L, L_{TS,HS} = 75$ μm), the radius of the helical microrobot ($R, R_{TS,HS} = 15.75$ μm), the pitch (separation between consecutive helical turns) of the helix (λ, $\lambda_{TS,HS} = 30$ μ), and the helix angle $\theta = \arctan(2\pi R/\lambda)$. In addition, N represents the number of turns of the helical microrobot ($N_{TS,HS} = 2.5$).

Since the motion in the fluid occurs in a low Re environment ($\mathrm{Re} < 10^{-3}$), our TS and HS motor performance study focuses on the advancing velocity and step-out frequency. Due to the boundary effect and frictional force, the advancing velocity is different from the absolute velocity, which is composed of the forwarding velocity and drift (lateral) velocity. The TS and HS step-out frequencies in DI water are approximately 30 and 25 Hz, and the maximum swimming speeds are approximately 272 and 144.6 μm/s, respectively.

B. Performance Assessment

Data Acquisition: Gets the controller design data set from the physical system. The angle $\theta \in (-\pi, \pi]$ between the magnetic field rotation axis and the horizontal line, selected

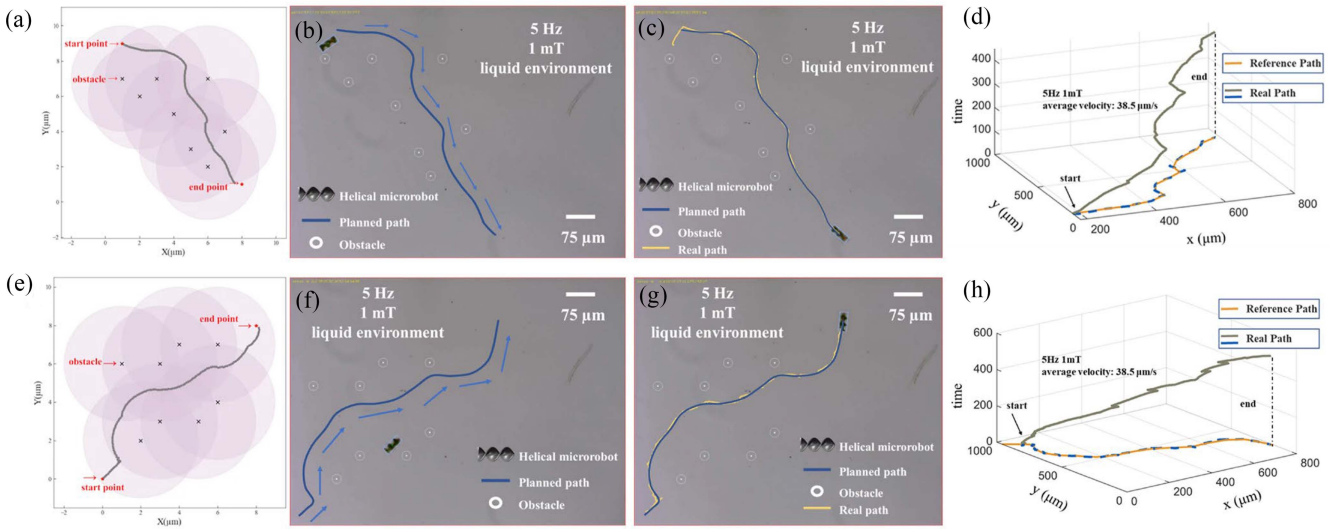

Fig. 13. Obstacle avoidance task using the D^2-OIC approach. The scale bar is 75 μm. (a) and (e) simulation results of path planning. (b), (c), (f), and (g) sequence of images of the experimental process. (d) and (h) trajectory data results of the helical microrobot.

clockwise and equally spaced angle values, was used as input data. The sampling frequency was set to 0.01 s. The barycenter coordinates of the TS were collected as output data. A total of 20 000 trajectory points were collected and divided into 62 data sets.

Data Enhancement: The least-squares rule was used to fit each set of trajectory points to make the trajectory representation. Eventually, SVR learned the mapping between the TS state data and the corresponding action from the demonstration (see Fig. 8). Eighty percent of the data were used for conditioning, using grid search and cross-validation, and the remaining 20% were used as a test set.

In this study, step response tests for the TS were conducted for three control groups: 1) open-loop control; 2) nonlinear control based on SVR; and 3) PID control. The experimental results are shown in Fig. 9. Under open-loop control, the TS deviates significantly from the excitation signal, with a maximum error of 57.6°. The nonlinear feedback control based on SVR makes the TS gradually converge to the excitation signal, but there is a jitter, and it gradually deviates from the preset direction, with an error of 10°. This reason is the dynamic transformation of the environment, which leads to disturbance changes. The PID controller makes the TS gradually converge to the expected direction, but the adjustment time is too long, and there is a jitter in the motion process.

In addition, a path-tracking task was performed in an apparently heterogeneous medium cotaining numerous and disorderly mobile impurities and even some impurities with magnetic particles (see Fig. 10). When the TS becomes entangled with the impurities, it causes the TS to deviate from the preset path. When the TS is attracted to an impurity, the TS becomes trapped in place. An unstructured bottom and the presence of small impurities will aggravate the trembling of TS.

Fig. 11 shows the physical experimental results of the TS on the solid–liquid cross-phase surface based on the D^2-OIC approach for the cascaded controller, including the linear and curvilinear path-tracking results. The position errors of various paths converge to near zero (see Fig. 11 and Supplementary movie S1).

Fig. 12 illustrates a plot of the distance error, which displays noticeable peaks and jitter, due to a false displacement caused by errors in the center of the helical microrobot extraction process. The actual center of gravity of a helical microrobot is often not the geometric center of the imaged region due to the heterogeneous material distribution and the projection of the camera. A more important reason lies in the unpredictable jitter behavior that accompanies the TS motion, as well as the dynamic changes in the motion environment, leading to some large perturbations during the experiment. Distance deviations occur when the controller adjusts the errors due to these perturbations. Moreover, Spintop motion and wobbling during barycenter extraction will cause false displacements. The same identification error occurs when a helical microrobot is mixed with impurities.

The obstacle avoidance task was carried out using the proposed D^2-OIC control method. In practical scenarios, avoiding obstacles can be challenging due to the complex circumstances involved. The proposed D^2-OIC control method is well suited for addressing complex obstacle scenarios, as it enables a helical microrobot to automatically follow a reference path and avoid obstacles. Fig. 13 depicts the precise trajectory tracking of the microrobot as it navigates through a simulated environment replete with virtual obstacles. The microrobots exhibit an average velocity of 38.5 μm/s. Further details regarding the experiment can be found in the Supplementary video S1.

C. Transfer Control Effect Evaluation

The inner updating scheme function adds new helical microrobot motion sample points to the original data, simultaneously providing a greater weight to the penalty coefficients so that the estimated curve more closely approximates the new sample points.

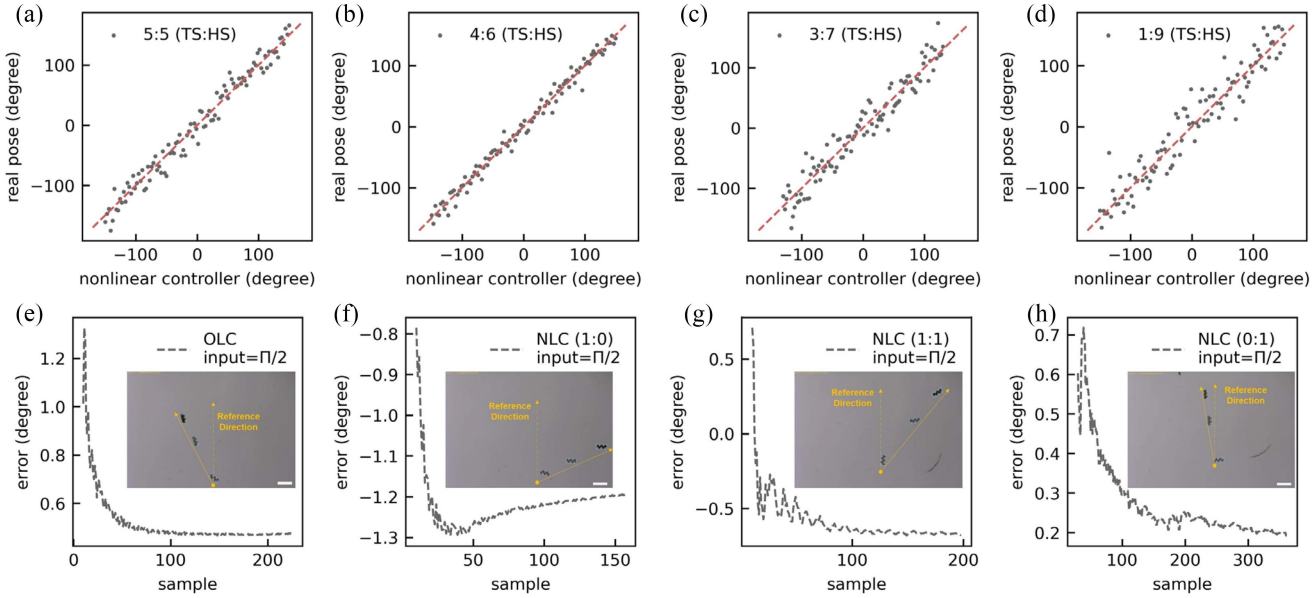

Fig. 14. (a)–(d) Adaptive transfer SVR training results graph. The horizontal axis corresponds to the controller signal, while the vertical axis represents the actual motion state. Additionally, the red line depicted in the graph signifies the diagonal line. Based on the original TS data: (a) Add HS data, with equal weight distribution. (b) With 4:6 (TS:HS) weight treatment. (c) With 3:7 (TS:HS) weight treatment. (d) With 1:9 (TS:HS) weight treatment. (e)–(h) HS trajectory under step signal stimulation with different controllers: (e) open loop controller, (f) nonlinear controller of the TS, (g) nonlinear controller based on adaptive transfer SVR with equal weight distribution, and (h) nonlinear controller of the HS.

Data Update: A set of data, used to update the control, was generated from the real system. A total of 20 sets new data were collected.

In this study, four sets of updated results are shown in Fig. 14. The nonlinear controller is subjected to various treatments, including the addition of new data with weight assignments of 1:1, 4:6, 3:7, and 1:9 (TS:HS) ratios. Then, a series of step tests were conducted, including open-loop controller, the TS nonlinear controller, and adaptive transfer nonlinear controllers [see Fig. 14(e)–(h)]. Based on the original TS control structure, adding a small amount of the HS test data, using our proposed transfer approach, the step response has a significant improvement effect, which confirms the effectiveness of the adaptive transfer control algorithm proposed in this article.

After testing, we chose 4:6 (TS:HS) for the control of the HS. Fig. 15 shows the straight and curved path-tracking results of the HS under adaptive control based on the D^2-OIC approach. The average values of the distance errors are 2.9 and 1.5 μm, which are significantly lower than the body length of the HS of approximately 75 μm, proving that the proposed method can accomplish a transfer control strategy (Supplementary movie S1).

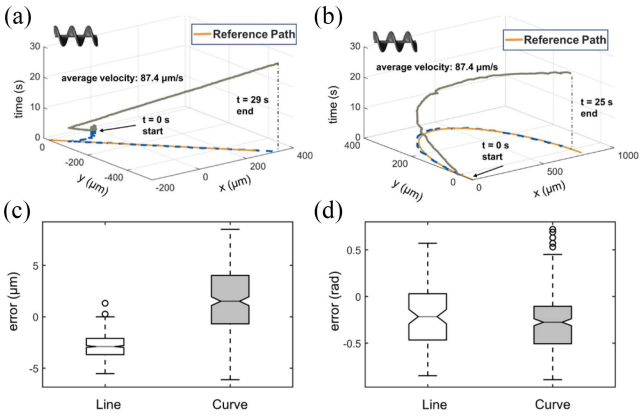

Fig. 15. Path-tracking experimental results of the HS. (a) Line path. (b) Curve path. (c) Distance error. (d) Yaw error.

VI. Conclusion

This work presents a method for precise and stable motion control of helical microrobots in microscale solid–liquid environments and a transfer control strategy among different types of helical microrobots. The control scheme is based on the D^2-OIC approach, which requires only a set of a helical microrobot experimental data to design their controllers without relying on their models. Experimental results show that helical microrobots can move along different path forms, including straight lines and curves. A modified SVR approach achieves transfer control for helical microrobots with different structures using a small amount of the new helical microrobot structure experimental data. These results demonstrate that the proposed method, rooted in data-driven and data-transfer method, offers a comprehensive and accurate automatic path-tracking control framework for helical microrobots, which has potential for motion control of microrobots with derived structures for different tasks.

With our proposed control method, precise planar motion control of diverse magnetic microrobots and their derived structures can be achieved. Furthermore, by obtaining the 3-D pose of the robot, this method can be readily extended

to enable accurate 3-D motion control of magnetic microrobots. In practical applications, our control method exhibits tremendous potential for facilitating targeted transport tasks within the biomedical field.

REFERENCES

[1] B. J. Nelson, S. Gervasoni, P. W. Y. Chiu, L. Zhang, and A. Zemmar, "Magnetically actuated medical robots: An in vivo perspective," *Proc. IEEE*, vol. 110, no. 7, pp. 1028–1037, Jul. 2022.

[2] Y. Dong et al., "Magnetic helical micro-/nanomachines: Recent progress and perspective," *Matter*, vol. 5, no. 1, pp. 77–109, Jan. 2022.

[3] J. Miao et al., "Flagellar/ciliary intrinsic driven mechanism inspired all-in-one tubular robotic actuator," *Engineering*, vol. 23, pp. 170–180, Apr. 2023, doi: 10.1016/j.eng.2022.09.014.

[4] I. S. M. Khalil et al., "Mechanical rubbing of blood clots using helical robots under ultrasound guidance," *IEEE Robot. Autom. Lett.*, vol. 3, no. 2, pp. 1112–1119, Apr. 2018.

[5] J. Leclerc et al., "In Vitro design investigation of a rotating helical magnetic swimmer for combined 3-D navigation and blood clot removal," *IEEE Trans. Robot.*, vol. 36, no. 3, pp. 975–982, Jun. 2020.

[6] Z. Wu, Y. Zhang, Z. Chi, and Q. Xu, "Design and development of a new rotating electromagnetic field generation system for driving microrobots," *IEEE Trans. Magn.*, vol. 58, no. 1, pp. 1–8, Jan. 2022.

[7] Q. Zou, X. Du, Y. Liu, H. Chen, Y. Wang, and J. Yu, "Dynamic path planning and motion control of microrobotic swarms for mobile target tracking," *IEEE Trans. Autom. Sci. Eng.*, vol. 20, no. 4, pp. 2454–2468, Oct. 2023, doi: 10.1109/TASE.2022.3207289.

[8] M. Ye, Y. Zhou, H. Zhao, and X. Wang, "Magnetic microrobots with folate targeting for drug delivery," *Cyborg Bionic Syst.*, vol. 4, May 2023, p. 19.

[9] D. Lin, W. Chen, K. He, N. Jiao, Z. Wang, and L. Liu, "Position and orientation control of multisection magnetic soft microcatheters," *IEEE/ASME Trans. Mechatron.*, vol. 28, no. 2, pp. 907–918, Apr. 2023.

[10] C. Huang, Z. Lai, X. Wu, and T. Xu, "Multimodal locomotion and cargo transportation of magnetically actuated quadruped soft microrobots," *Cyborg Bionic Syst.*, vol. 2022, p. 4, Jan. 2022.

[11] L. Yang and L. Zhang, "Motion control in magnetic microrobotics: From individual and multiple robots to swarms," *Annu. Rev. Control Robot. Auton. Syst.*, vol. 4, no. 1, pp. 509–534, May 2021.

[12] D. Schamel et al., "Nanopropellers and their actuation in complex viscoelastic media," *ACS Nano*, vol. 8, no. 9, pp. 8794–8801, Sep. 2014.

[13] M. C. Hoang et al., "Independent electromagnetic field control for practical approach to actively locomotive wireless capsule endoscope," *IEEE Trans. Syst., Man, Cybern.*, Syst., vol. 51, no. 5, pp. 3040–3052, May 2021.

[14] S. Tottori et al., "Magnetic helical micromachines: Fabrication, controlled swimming, and cargo transport," *Adv. Mater.*, vol. 24, no. 6, pp. 811–816, Feb. 2012.

[15] H.-S. Lee, J. Back, and C.-S. Kim,, "Disturbance observer-based robust controller for a multiple-electromagnets actuator," *IEEE Trans. Ind. Electron.*, vol. 71, no. 1, pp. 901–911, Jan. 2024, doi: 10.1109/TIE.2023.3247740.

[16] A. Ghanbari and M. Bahrami, "Nonlinear modeling application to micro-/nanorobotics," in *Nonlinear Approaches in Engineering Applications: Automotive Applications of Engineering Problems*, R. N. Jazar and L. Dai, Eds. Cham, Switzerland: Springer Int. Publ., 2020, pp. 113–140.

[17] A. Barbot, D. Decanini, and G. Hwang, "Local flow sensing on helical microrobots for semi-automatic motion adaptation," *Int. J. Robot. Res.*, vol. 39, no. 4, pp. 476–489, Mar. 2019.

[18] S. Lee et al., "A needle-type microrobot for targeted drug delivery by affixing to a microtissue," *Adv. Healthc. Mater.*, vol. 9, no. 7, Mar. 2020, Art. no. 1901697.

[19] H. Cao et al., "Image-guided corridor-based motion planning and magnetic control of microrotor in dynamic environments," *IEEE/ASME Trans. Mechatron.*, vol. 27, no. 6, pp. 5415–5426, Dec. 2022.

[20] S. Zhong et al., "Spatial constraint-based navigation and emergency replanning adaptive control for magnetic helical microrobots in dynamic environments," *IEEE Trans. Autom. Sci. Eng.*, early access, Dec. 20, 2023, doi: 10.1109/TASE.2023.3339637.

[21] Z. Xie, L. Jin, X. Luo, B. Hu, and S. Li, "An acceleration-level data-driven repetitive motion planning scheme for kinematic control of robots with unknown structure," *IEEE Trans. Syst., Man, Cybern., Syst.*, vol. 52, no. 9, pp. 5679–5691, Sep. 2022.

[22] C. Novara, S. Formentin, S. M. Savaresi, and M. Milanese, "Data-driven design of two degree-of-freedom nonlinear controllers: The D^2-IBC approach," *Automatica*, vol. 72, pp. 19–27, Oct. 2016.

[23] C. Novara and S. Formentin, "Data-driven inversion-based control of nonlinear systems with guaranteed closed-loop stability," *IEEE Trans. Autom. Control*, vol. 63, no. 4, pp. 1147–1154, Apr. 2018.

[24] X. Yu, Z. Hou, and M. M. Polycarpou, "Controller-dynamic-linearization-based data-driven ILC for nonlinear discrete-time systems with RBFNN," *IEEE Trans. Syst., Man, Cybern., Syst.*, vol. 52, no. 8, pp. 4981–4992, Aug. 2022.

[25] X. Ren, Y. Liu, Y. Hu, and Z. Li, "Integrated task sensing and whole body control for mobile manipulation with series elastic actuators," *IEEE Trans. Autom. Sci. Eng.*, vol. 20, no. 1, pp. 413–424, Jan. 2023.

[26] Z. Li, W. Yuan, Y. Chen, F. Ke, X. Chu, and C. L. P. Chen, "Neural-dynamic optimization-based model predictive control for tracking and formation of nonholonomic multirobot systems," *IEEE Trans. Neural Netw. Learn. Syst.*, vol. 29, no. 12, pp. 6113–6122, Dec. 2018.

[27] F. Ke, Z. Li, and C. Yang, "Robust tube-based predictive control for visual servoing of constrained differential-drive mobile robots," *IEEE Trans. Ind. Electron.*, vol. 65, no. 4, pp. 3437–3446, Apr. 2018.

[28] X. Wu, J. Liu, C. Huang, M. Su, and T. Xu, "3-D path following of helical microswimmers with an adaptive orientation compensation model," *IEEE Trans. Autom. Sci. Eng.*, vol. 17, no. 2, pp. 823–832, Apr. 2020.

[29] T. Xu et al., "Discrete-time optimal control of miniature helical swimmers in horizontal plane," *IEEE Trans. Autom. Sci. Eng.*, vol. 19, no. 3, pp. 2267–2277, Jul. 2022.

[30] S. Zhong et al., "Double-modal locomotion of a hydrogel ultra-soft magnetic miniature robot with switchable forms," *Cyborg Bionic Syst.*, vol. 5, Jan. 2024, p. 0077, doi: 10.34133/CBSYSTEMS.0077.

[31] X. Wang, C. Hu, S. Pané, and B. J. Nelson, "Dynamic modeling of magnetic helical microrobots," *IEEE Robot. Autom. Lett.*, vol. 7, no. 2, pp. 1682–1688, Apr. 2022.

[32] T. Xu, Y. Guan, J. Liu, and X. Wu, "Image-based visual servoing of helical microswimmers for planar path following," *IEEE Trans. Autom. Sci. Eng.*, vol. 17, no. 1, pp. 325–333, Jan. 2020.

[33] V. Vapnik, *Statistical Learning Theory*. New York, NY, USA: Wiley, 1998.

[34] D. Zhang and J. Lei, "Kinematic analysis of a novel 3-DOF actuation redundant parallel manipulator using artificial intelligence approach," *Robot. Comput.-Integr. Manuf.*, vol. 27, no. 1, pp. 157–163, 2011.

[35] B. Xu, H. Zhu, and X. Wang, "Decoupling control of outer rotor coreless bearingless permanent magnet synchronous motor based on least squares support vector machine generalized inverse optimized by improved genetic algorithm," *IEEE Trans. Ind. Electron.*, vol. 69, no. 12, pp. 12182–12190, Dec. 2022, doi: 10.1109/TIE.2021.3130345.

[36] A. Carè et al., "A toolbox for virtual reference feedback tuning (VRFT)," in *Proc. 18th Eur. Control Conf.*, 2019, pp. 4252–4256.

[37] M. Campi, A. Lecchini, and S. M. Savaresi, "Virtual reference feedback tuning: A direct method for the design of feedback controllers," *Automatica*, vol. 38, no. 8, pp. 1337–1346, 2002.

[38] C. Zhou et al., "A new model transfer strategy among spectrometers based on SVR parameter calibrating," *IEEE Trans. Instrum. Meas.*, vol. 70, pp. 1–13, 2021.

[39] Y. Hou et al., "Design and control of a surface-dimple-optimized helical microdrill for motions in high-viscosity fluids," *IEEE/ASME Trans. Mechatron.*, vol. 28, no. 1, pp. 429–439, Feb. 2023.

Huaping Wang (Member, IEEE) received the B.S. degree in mechatronics and the Ph.D. degree in mechanical engineering from the Beijing Institute of Technology, Beijing, China, in 2010 and 2015, respectively.

He has been a Professor with the Beijing Institute of Technology since 2022. His research interests include micro–nano robotics, micro–nano manipulation, and automation at micro–nano scales.

Shihao Zhong received the B.S. degree in automation from the North China University of Technology, Beijing, China, in 2021. He is currently pursuing the Ph.D. degree in mechanical engineering with the Beijing Institute of Technology, Beijing.

His research interests include navigation control of micro/nano machines.

Zhiqiang Zheng received the B.S. degree in engineering from the Hebei University of Technology, Tianjin, China, in 2015, the M.S. degree in engineering from the University of Nottingham, Nottingham, U.K., in 2017, and the Ph.D. degree in engineering from the School of Mechanical and Electrical Engineering, Beijing Institute of Technology, Beijing, China, in 2021.

He has been a Postdoctoral Scientist of Physical Intelligence with Max Planck Institute, Stuttgart, Germany, since 2021. His research interests include microrobot, soft robotic, smart materials, and magnetic robot.

Qing Shi (Senior Member, IEEE) received the B.S. degree in mechatronics from the Beijing Institute of Technology, Beijing, China, in 2006, and the Ph.D. degree in biomedical engineering from Waseda University, Tokyo, Japan, in 2012.

He was a Research Associate with the GCOE Global Robot Academia, Waseda University from 2009 to 2013. He is currently a Professor with the School of Mechatronical Engineering, Beijing Institute of Technology. His research interests are focused on bio-inspired robots, computer vision, and micro/nano robotics.

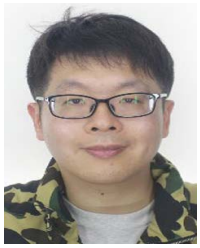

Tao Sun received the Ph.D. degree in mechanical engineering from the Beijing Institute of Technology, Beijing, China, in 2016.

His research interests include applications of biofabrication and biomanipulation in micro–nano scale.

Qiang Huang (Fellow, IEEE) received the B.S. and M.S. degrees in electrical engineering from the Harbin Institute of Technology, Harbin, China, in 1986 and 1989, respectively, and the Ph.D. degree in mechanical engineering from Waseda University, Tokyo, Japan, in 1996.

He was a Research Fellow with the National Institute of Advanced Industrial Science and Technology, Tokyo, from 1996 to 1999. He was a Research Fellow with the University of Tokyo, Tokyo, from 1999 to 2000. He is currently a Professor with the Beijing Institute of Technology, Beijing, China, where he is also the Director of the Key Laboratory of Biomimetic Robots and Systems, Ministry of Education.

Prof. Huang received the First-Class Prize of the Ministry of Education Award for Technology Invention. He serves as the Chair in many IEEE conferences, such as the Organizing Committee Chair of the 2006 IEEE/RSJ International Conference on Intelligent Robots and Systems, the General Chair of the 2017 IEEE International Conference on Robotics and Biomimetics, and the 2018 IEEE-RAS International Conference on Humanoid Robots.

Toshio Fukuda (Life Fellow, IEEE) received the B.S. degree in engineering from Waseda University, Tokyo, Japan, in 1971, and the M.S. and Ph.D. degrees in engineering from the University of Tokyo, Tokyo, in 1973 and 1977, respectively.

He is currently a Professor (1000 Foreign Experts Plan) with the Intelligent Robotics Institute, School of Mechatronic Engineering, Beijing Institute of Technology, Beijing, China, where he is mainly engaged in the research fields of intelligent robotic systems, cellular robotic systems, mechatronics, and micro/nano robotics. From 1977 to 1982, he was with the National Mechanical Engineering Laboratory, Tsukuba, Japan. From 1982 to 1989, he was with the Science University of Tokyo, Tokyo. Starting in 1989, he was with Nagoya University, Nagoya, Japan, where he was a Professor with the Department of Micro System Engineering, and a Professor with Meijo University, Nagoya.

Dr. Fukuda was the President of the IEEE Robotics and Automation Society from 1998 to 1999, the Editor-in-Chief of IEEE/ASME TRANSACTIONS ON MECHATRONICS from 2000 to 2002, the Director of Division X: Systems and Control from 2001 to 2002, the IEEE Founding President of Nanotechnology Council from 2002 to 2003 and in 2005, the Director of Region 10 from 2013 to 2014, and the Director of Division X: Systems and Control from 2017 to 2018.